ACS NANO

www.acsnano.org

ARTICLE

Doping the Undopable: Hybrid Molecular Beam Epitaxy Growth, n-Type Doping, and Field-Effect Transistor Using $CaSnO_3$

Fengdeng Liu, Prafful Golani, Tristan K. Truttmann, Igor Evangelista, Michelle A. Smeaton, David Bugallo, Jiaxuan Wen, Anusha Kamath Manjeshwar, Steven J. May, Lena F. Kourkoutis, Anderson Janotti, Steven J. Koester,* and Bharat Jalan*

Cite This: *ACS Nano* 2023, 17, 16912−16922

Read Online

ACCESS | Metrics & More | Article Recommendations | Supporting Information

ABSTRACT: **The alkaline earth stannates are touted for their wide band gaps and the highest room-temperature electron mobilities among all of the perovskite oxides. $CaSnO_3$ has the highest measured band gap in this family and is thus a particularly promising ultrawide band gap semiconductor. However, discouraging results from previous theoretical studies and failed doping attempts had described this material as "undopable". Here we redeem $CaSnO_3$ using hybrid molecular beam epitaxy, which provides an adsorption-controlled growth for the phase-pure, epitaxial, and stoichiometric $CaSnO_3$ films. By introducing lanthanum (La) as an n-type dopant, we demonstrate the robust and predictable doping of $CaSnO_3$ with free electron concentrations, n_{3D}, from 3.3×10^{19} cm^{-3} to 1.6×10^{20} cm^{-3}. The films exhibit a maximum room-temperature mobility of 42 cm^2 V^{-1} s^{-1} at $n_{3D} = 3.3 \times 10^{19}$ cm^{-3}. Despite having a comparable radius as the host ion, La expands the lattice parameter. Using density functional calculations, this effect is attributed to the energy gain by lowering the conduction band upon volume expansion. Finally, we exploit robust doping by fabricating $CaSnO_3$-based field-effect transistors. The transistors show promise for $CaSnO_3$'s high-voltage capabilities by exhibiting low off-state leakage below 2×10^{-5} mA/mm at a drain−source voltage of 100 V and on−off ratios exceeding 10^6. This work serves as a starting point for future studies on the semiconducting properties of $CaSnO_3$ and many devices that could benefit from $CaSnO_3$'s exceptionally wide band gap.**

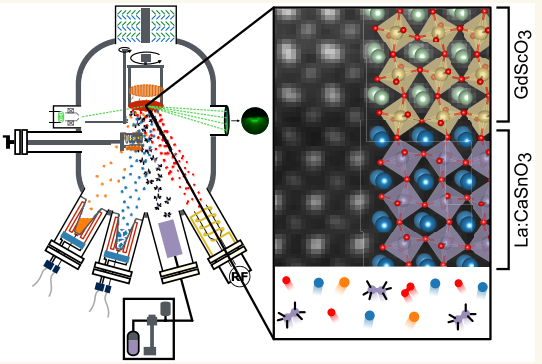

KEYWORDS: *ultrawide band gap (UWBG) semiconductors, hybrid molecular beam epitaxy (hMBE), calcium stannate, chemical doping, density functional calculations, metal−semiconductor field-effect transistor (MESFET), high-voltage electronics*

Downloaded via CORNELL UNIV on February 2, 2024 at 03:26:05 (UTC).
See https://pubs.acs.org/sharingguidelines for options on how to legitimately share published articles.

INTRODUCTION

Alkaline earth stannates have been among the most exciting materials for research in the past decade, due to their wide band gaps and their high room-temperature electron mobilities.[1] In particular, $BaSnO_3$ has a band gap of 3.1 eV[2,3] and room-temperature electron mobility as high as 320 cm^2 V^{-1} s^{-1} in bulk single crystals, the highest among all perovskite oxides.[1] Thin-film $BaSnO_3$, however, has achieved a mobility of only 183 cm^2 V^{-1} s^{-1}.[4] Researchers attribute this discrepancy to the high density of threading dislocations resulting from the large lattice mismatch with commercially available substrates.[5,6] Replacing Ba with the smaller Sr to counter the lattice mismatch produces $SrSnO_3$ with a wider band gap of 4.1 eV[2,3] and a room-temperature mobility as high as 72 cm^2 V^{-1} s^{-1} in thin films.[7] These make $SrSnO_3$ an attractive ultrawide band gap (UWBG) semiconductor for high-performance radio frequency (RF) devices.[8,9] Even though $SrSnO_3$ can be grown coherently on $GdScO_3$ (110) substrates due to its smaller lattice parameter,[10−12] above a critical thickness of 12−26 nm, a structural phase transition and subsequent strain relaxation lead to substantial structural degradation.[7] Additionally, $SrSnO_3$ is also sensitive to temperature,[13] composition,[14] and biaxial strain,[11] which complicates its implementation in devices.

Received: May 4, 2023
Accepted: August 21, 2023
Published: August 28, 2023

© 2023 American Chemical Society

https://doi.org/10.1021/acsnano.3c04003
ACS Nano 2023, 17, 16912−16922

$CaSnO_3$ inherently overcomes the lack of lattice matched substrates (in the case of $BaSnO_3$) and structural sensitivity (in the case of $SrSnO_3$). It is remarkably comfortable in its orthorhombic structure (shown in Figure 1a), insensitive to

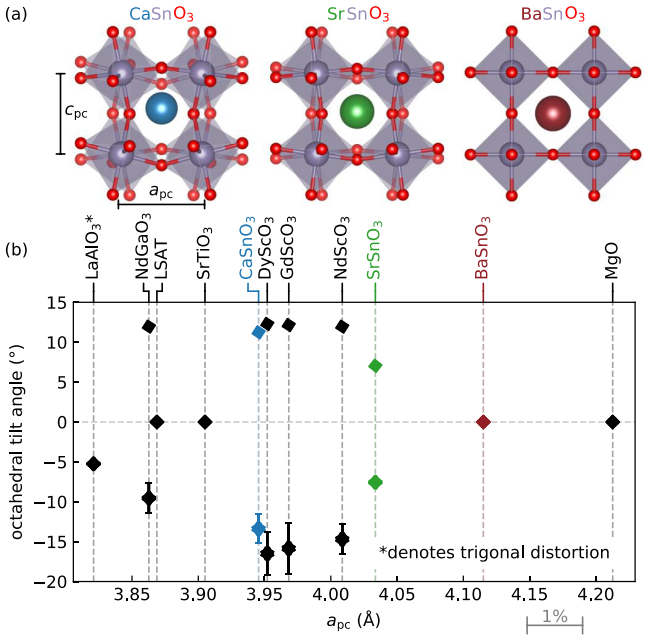

Figure 1. (a) Crystal structures of the alkaline earth stannates ($CaSnO_3$, $SrSnO_3$, and $BaSnO_3$) from Mountstevens *et al.*[14] (b) Pseudocubic lattice parameters (a_{pc}) and octahedral tilt angles of the stannates and commercially available single-crystal substrates. Tilt angles were calculated using the B−B−B−O dihedral angles, shown with positive angles representing in-phase tilts and negative angles representing antiphase tilts. The error bars represent ambiguity in the angles due to octahedral distortions.

extreme temperatures,[15] pressures,[16] and compositional changes.[14] Only under the exceptionally extreme conditions of 2000 K and 50 GPa does $CaSnO_3$ exhibit a phase transition out of its orthorhombic symmetry into an edge-sharing postperovskite structure.[17] Replacing Ba or Sr with Ca further decreases the pseudocubic lattice parameter of $CaSnO_3$ to a_{pc} = 3.95 Å,[14] putting its lattice parameter closer to several commercially available perovskite oxide substrates with the same space group and similar octahedral tilt angles (Figure 1b).[14,18] These qualities suggest that epitaxial $CaSnO_3$ might achieve structural quality akin to that typically achieved in homoepitaxial perovskites. The small Ca^{2+} A-site cation also achieves the largest octahedral tilt angles of the three stannates, as shown in Figure 1b. This decreases the conduction band dispersion, enlarging the band gap to 4.4 eV.[2,3] The Baliga figure of merit (BFOM), which quantifies a material's suitability for power electronics, is proportional to the band gap cubed.[19] Therefore, this small increase in the band gap potentially gives $CaSnO_3$ a substantial advantage over $SrSnO_3$.

Despite all of these promising fundamental properties, $CaSnO_3$'s *semiconducting* properties have been, until now, unrealized. Wei *et al.* grew 3% La-doped $CaSnO_3$ by pulsed laser deposition (PLD) in an attempt to characterize its semiconducting properties, but the films did not exhibit measurable conductivity despite $SrSnO_3$ and $BaSnO_3$ achieving robust conductivity under similar growth conditions.[20] Perhaps this result was unsurprising given that Weston *et al.* had already warned that "doping [$CaSnO_3$] looks particularly challenging"[21] from their theoretical studies. Shaili *et al.* have arguably achieved Nd doping in polycrystalline $CaSnO_3$ films, but the room-temperature mobility remained <4 $cm^2\ V^{-1}\ s^{-1}$.[22]

Here, by growing $CaSnO_3$ on $GdScO_3$ (110) substrates within an adsorption-controlled growth window using hybrid molecular beam epitaxy, we show that $CaSnO_3$ not only can be doped but can achieve *robust and predictable* doping that spans a 5-fold range of carrier concentrations. It is noted that despite having ideally lattice-matched $DyScO_3$ (110) substrates, $GdScO_3$ substrates were chosen due to their low lattice mismatch and tilt mismatch (Figure 1b) because it allows for the unambiguous determination of the out-of-plane lattice parameter of films owing to distinct peaks from the film and the substrate.

Good room-temperature mobilities can also be achieved up to 42 $cm^2\ V^{-1}\ s^{-1}$. In addition, we demonstrate the potential of this UWBG semiconductor by fabricating field-effect transistors (FETs) that use $CaSnO_3$ as the channel material. The transistors exhibit an on−off ratio exceeding 10^6 and off-state leakage below 10^{-6} mA/mm at a drain−source voltage (V_{DS}) of 1 V, attesting to the high degree of doping control. The transistors also exhibit outstanding high-voltage capabilities, with off-state leakage of $<2 \times 10^{-5}$ mA/mm at a source−drain voltage of 100 V, demonstrating $CaSnO_3$'s promise for high-voltage devices. We conclude by discussing why our doping attempts have succeeded, whereas previous attempts have failed.

RESULTS

We begin our study of $CaSnO_3$ by growing 65 nm La:$CaSnO_3$ on a $GdScO_3$ (110) substrate. Here, we fixed the Ca flux and varied hexamethylditin (HMDT) to achieve different HMDT/Ca beam equivalent pressure (BEP) ratios ranging from 877 to 1158 to explore cation stoichiometry. La flux was also kept unchanged by fixing La-cell temperature. The reflection high energy electron diffraction (RHEED) patterns in Figure S1 exhibit tall streaks, which indicate a smooth surface, bright half-order streaks, which correspond to the unit-cell doubling caused by $CaSnO_3$'s large octahedral tilting, and Kikuchi lines, which indicate high crystalline quality, all three of which show no discernible dependence on BEP ratio. The representative atomic force micrograph in Figure S2 has an RMS surface roughness of 227 pm, consistent with the streaky RHEED images. The high-resolution X-ray diffraction (HRXRD) coupled scans of these samples show clear Laue oscillations, which demonstrate uniform films with a high structural quality (Figure 2a). The film rocking curves shown in Figure S3 exhibit full widths at halfmaximum (FWHM) of 0.024−0.038°, with no clear dependence on BEP ratio. These are broader than the substrate rocking curves (FWHM ≈ 0.006°), but are at least 7-fold narrower than the narrowest film rocking curve (FWHM = 0.27°) in the existing $CaSnO_3$ literature.[23]

From the HRXRD coupled scans, we calculated the out-of-plane lattice parameters c_{pc} of the La:$CaSnO_3$ films grown under different BEP ratios, as shown in Figure 2b. We found that c_{pc} of all the films showed no obvious dependence on the BEP ratio, a behavior dissimilar to $BaSnO_3$, where a Sn deficiency manifests as an expanded lattice parameter.[24] More surprisingly, the film lattice parameters were very close to the bulk lattice parameter (within 0.04%), despite being tensile-strained (0.38%) to the $GdScO_3$ substrate indicated by the reciprocal space map of the $(103)_{pc}$ region in the inset of

https://doi.org/10.1021/acsnano.3c04003
ACS Nano 2023, 17, 16912−16922

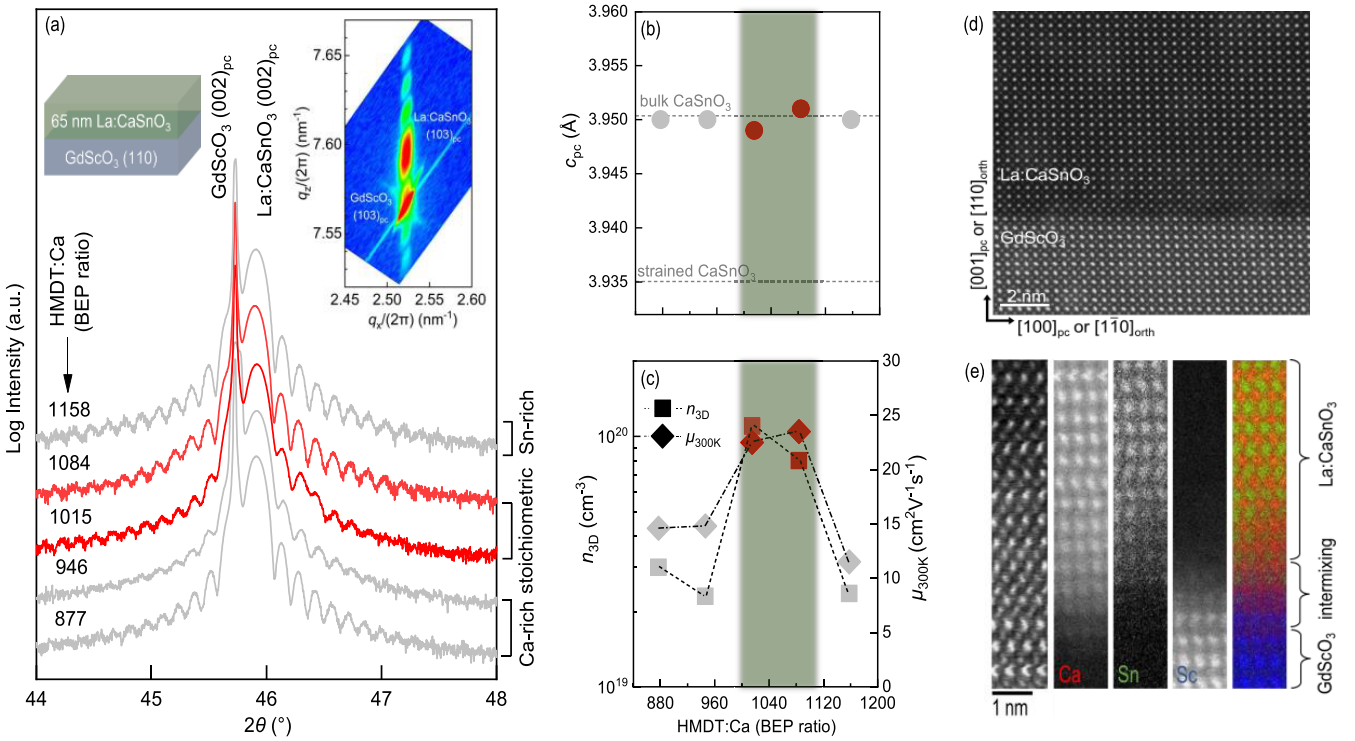

Figure 2. (a) High-resolution X-ray diffraction $2\theta-\omega$ coupled scans of 65 nm La:$CaSnO_3$/$GdScO_3$ (110) grown with different HMDT:Ca BEP ratios. The left-side inset shows a schematic of the sample structure. The right-side inset shows an asymmetric reciprocal space map around the $(103)_{pc}$ reflection for a BEP ratio = 1015. (b) Out-of-plane pseudocubic lattice parameters, c_{pc}, for different BEP ratios. Dashed lines indicate the out-of-plane pseudocubic lattice parameter corresponding to the bulk $CaSnO_3$ and a fully strained $CaSnO_3$ film on a $GdScO_3$ (110) substrate. (c) Room-temperature carrier concentrations n_{3D} and mobilities μ_{300K} plotted against the BEP ratio. (d) Cross-sectional HAADF-STEM of the La:$CaSnO_3$/$GdScO_3$ interface for BEP ratio = 1015, imaged along the $[001]_{orth}$ zone axis (e) STEM electron energy loss spectroscopy (EELS) elemental maps showing intermixing between the $GdScO_3$ substrate and La:$CaSnO_3$ film.

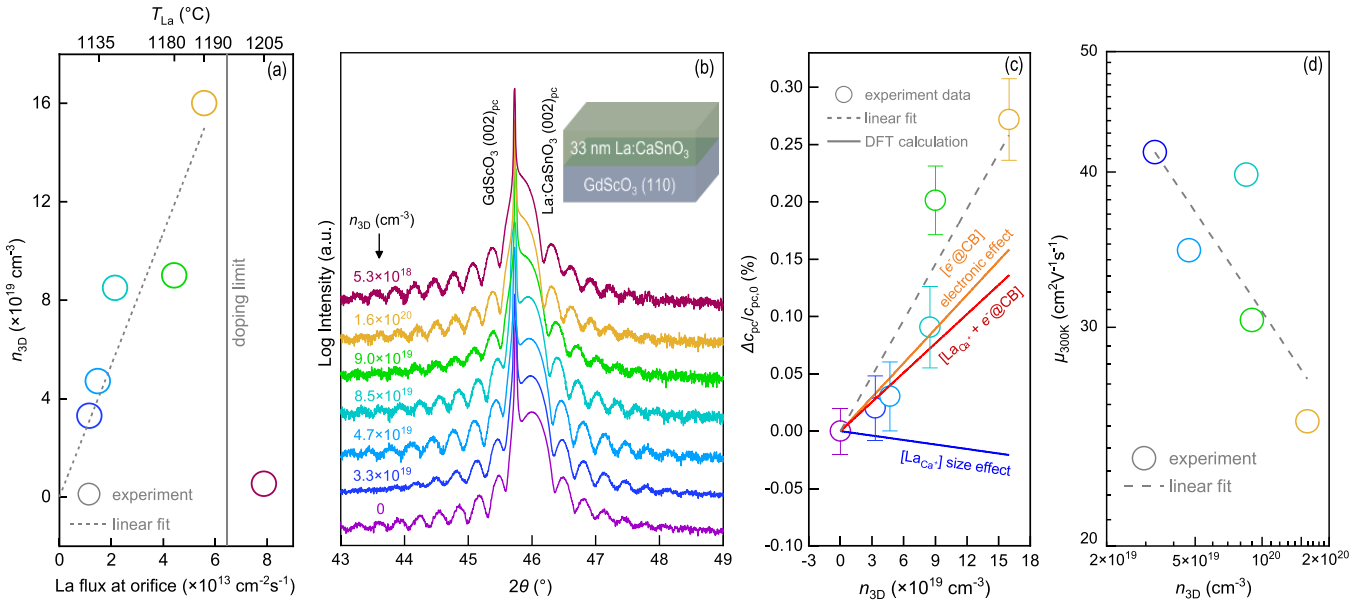

Figure 3. (a) Room-temperature carrier concentration n_{3D} as a function of the La flux at the crucible orifice, controlled by the effusion cell temperature. A proportional fit to the data is shown with a dashed line. (b) High-resolution X-ray diffraction $2\theta-\omega$ coupled scans of La:$CaSnO_3$/$GdScO_3$(110) with various carrier concentrations n_{3D}. The inset shows a schematic of the sample structure. (c) Expansion of the out-of-plane lattice parameter Δc_{pc} with respect to $c_{pc,0}$ (undoped lattice parameter) as a function of the carrier concentration n_{3D}. The experimental data points are shown as circles with a proportional fit shown with a dashed line. DFT predictions are shown as solid lines including the La size effect, the electronic effect, and the two effects together. (d) Room-temperature electron mobility μ_{300K} as a function of the carrier concentration n_{3D}. A guide to the eye is shown as a dashed line.

https://doi.org/10.1021/acsnano.3c04003
ACS Nano 2023, 17, 16912−16922

Figure 2a. We later explain that the expanded lattice parameters is because of electronic carrier-induced lattice expansion.

To probe the cation stoichiometry of the films more sensitively, we performed room-temperature Hall measurements of the films and extracted the carrier concentrations (n_{3D}) and mobilities (μ_{300K}) as a function of the HMDT/Ca BEP ratio, shown in Figure 2c. At extreme BEP ratios, the mobilities are relatively low (12−15 $cm^2\ V^{-1}\ s^{-1}$), whereas at intermediate BEP ratios, the mobilities are much higher (22−24 $cm^2\ V^{-1}\ s^{-1}$), a trend similar to $BaSnO_3$[24] and $SrSnO_3$.[10] The carrier concentration also shows a similar trend. These intermediate BEP ratios between 1015 and 1084 constitute a growth window represented by the green shaded region in Figure 2c, in which the 1:1 Sn:Ca cation stoichiometry is self-regulated and thus impervious to flux instabilities. Here, the higher HMDT/Ca BEP ratios refer to Sn-rich growth conditions, whereas the lower HMDT/Ca BEP ratios indicate Ca-rich conditions. Whether the decrease in n_{3D} and μ_{300K} (outside the growth window) is related to Ca- or Sn-vacancies or related defect complexes remains unclear and should be investigated using more sensitive techniques such as positron annihilation.

Figure 2d shows a high-angle annular dark-field scanning transmission electron microscopy (HAADF-STEM) image of the La:$CaSnO_3$/$GdScO_3$(110) interface down the $[001]_{orth}$ zone axis for the sample growth with a BEP ratio = 1015. The image shows a clearly epitaxial relationship and a coherent interface consistent with the RSM map. The Ca and Gd columns are both elliptical, reflecting the A-site alternating displacements, which are visible only in the $[001]_{orth}$ zone axis. This indicates a $(110)_{orth}||(110)_{orth}$ and $[001]_{orth}||[001]_{orth}$ epitaxial relationship. Consistent with a fully strained film, these results combined with a low-resolution STEM HAADF image (Figure S4) reveal no measurable dislocations. The reader may wonder, why does the polar discontinuity between locally polar $GdScO_3$ and nonpolar $CaSnO_3$ produce a two-dimensional carrier gas? The STEM electron energy loss spectroscopy (EELS) maps in Figure 2e and the additional analysis in Figure S4 show that there is significant intermixing between the substrate and film cations. This likely results from using untreated substrates that do not exhibit an atomically abrupt surface or preferential surface termination. This intermixing prevents the abrupt interface required to produce the polar discontinuity, which leads to the formation of a two-dimensional carrier gas. Future studies might explore the possibility of growing $CaSnO_3$ on rare earth scandate substrates treated to achieve an atomically abrupt surface with defined A-site or B-site termination.[25,26]

Whereas, in the previous section, we used various BEP ratios and a fixed La effusion cell temperature of T_{La} = 1190 °C to optimize the cation stoichiometry, we now show results from films grown with a fixed BEP ratio of 1015 (inside the growth window) and T_{La} varying from 1120 to 1205 °C to study doping. Figure 3a shows the n_{3D} as a function of the La flux at the crucible orifice, calculated from the kinetic theory of gases as done previously for Nd:$SrSnO_3$.[27] The film grown at T_{La} = 1120 °C did not show measurable conductivity. There are no reliable measurements or calculations of $CaSnO_3$'s effective mass, m^*, or dielectric constant, ε_r, so the Mott critical carrier concentration n_c cannot be calculated with great accuracy.[28] However, using m^* and ε_r of $BaSnO_3$ (m^* = 0.2−0.4m_e and ε_r = 20)[29,30] and $SrSnO_3$ (m^* = 0.3−0.4m_e and ε_r = 17),[11] reasonable inclusive ranges of $0.3 < m^*/m_e < 0.5$ and $10 < \varepsilon_r < 20$ yield a range of $4.0 \times 10^{17}\ cm^{-3} < n_c < 1.5 \times 10^{19}\ cm^{-3}$, which is much lower than the minimum n_{3D} in Figure 3a. Therefore, the lack of conductivity at T_{La} = 1120 °C must be explained by another mechanism, such as compensation or localization of the free carriers. The plot of the conductive samples in Figure 3a shows two regions. In the region to the *left* of T_{La} = 1195 °C, the data can be modeled by a straight line with a *y*-intercept of zero. This is strong evidence of 100% doping activation and one-to-one correlation between dopant concentration and carrier density. It is noted that La concentration in our films varies between 0.19 and 1.0 at. %. Since the nature of intrinsic defects is unclear, we do not express La concentration using a chemical formula such as $Ca_{1-x}La_xSnO_3$. In the region to the *right* of T_{La} = 1195 °C, the film shows the lowest n_{3D} of all the films, despite being grown at the highest T_{La}. This suggests a doping limit of $\sim 1.6 \times 10^{20}\ cm^{-3}$, above which La dopants either aggregate to form a secondary phase such as pyrochlore-type $La_2Sn_2O_7$[31] or self-compensate by occupying the Sn site.[21] Regardless of the mechanism behind the doping limit, the carrier concentrations from $3.3 \times 10^{19}\ cm^{-3}$ to $1.6 \times 10^{20}\ cm^{-3}$ in the left-side region of Figure 3a provide a 5-fold range of controlled carrier concentrations that can be used in electronic devices.

Before discussing our $CaSnO_3$ devices, however, we first discuss the structural changes resulting from the free electrons and their mobilities with doping. The rocking curves for these films, shown in Figure S5, exhibit FWHM values that vary from 0.026° to 0.041°, suggesting high structural quality that is not degraded by doping. Figure 3b shows the HRXRD coupled scans of these films. The patterns are mostly identical, the only discernible trend being that the film peaks coalesce with those of the substrate when $T_{La} \geq 1180$ °C, indicating that doping expands the lattice parameter. To extract the lattice parameters of these thinner films, we simulate their diffraction patterns with GenX 3;[32] the fits are shown in Figure S6a and the extracted lattice parameters are plotted versus n_{3D} in Figure S6b. This expansion with doping explains why the films described in Figure 2b exhibit bulklike out-of-plane lattice parameters despite being tensile-strained to $GdScO_3$. However, this lattice expansion is somewhat surprising given the comparable radius of La^{3+} compared to that of Ca^{2+} in the 12-fold coordination environment, as shown in Figure S7, which suggests that another mechanism, perhaps electronic, is at play.

To disentangle the ionic size and electronic effects on the lattice parameters, we turn to density functional theory (DFT). We find that adding one electron to the conduction band of the epitaxially strained $CaSnO_3$ leads to an increase in the out-of-plane *c* lattice parameter (pure electronic effect), whereas adding La without the extra electron leads to a decrease in the *c* lattice parameter (size effect), as shown in Figure 3c. The combined electronic and size effects, simulated by adding both La and its extra electron, result in a net expansion of the lattice, also shown in Figure 3c, in agreement with the trend we observed in our experiments. The effect of lattice expansion upon doping is attributed to the lowering of the conduction band minimum (CBM) as the volume increases. This arises from the negative value of the conduction band absolute deformation potential;[33,34] that is, as the volume increases, the CBM is lowered in an absolute energy scale due to its antibonding nature. If the conduction band edge states are occupied through doping, then the whole crystal lowers its

https://doi.org/10.1021/acsnano.3c04003
ACS Nano 2023, 17, 16912−16922

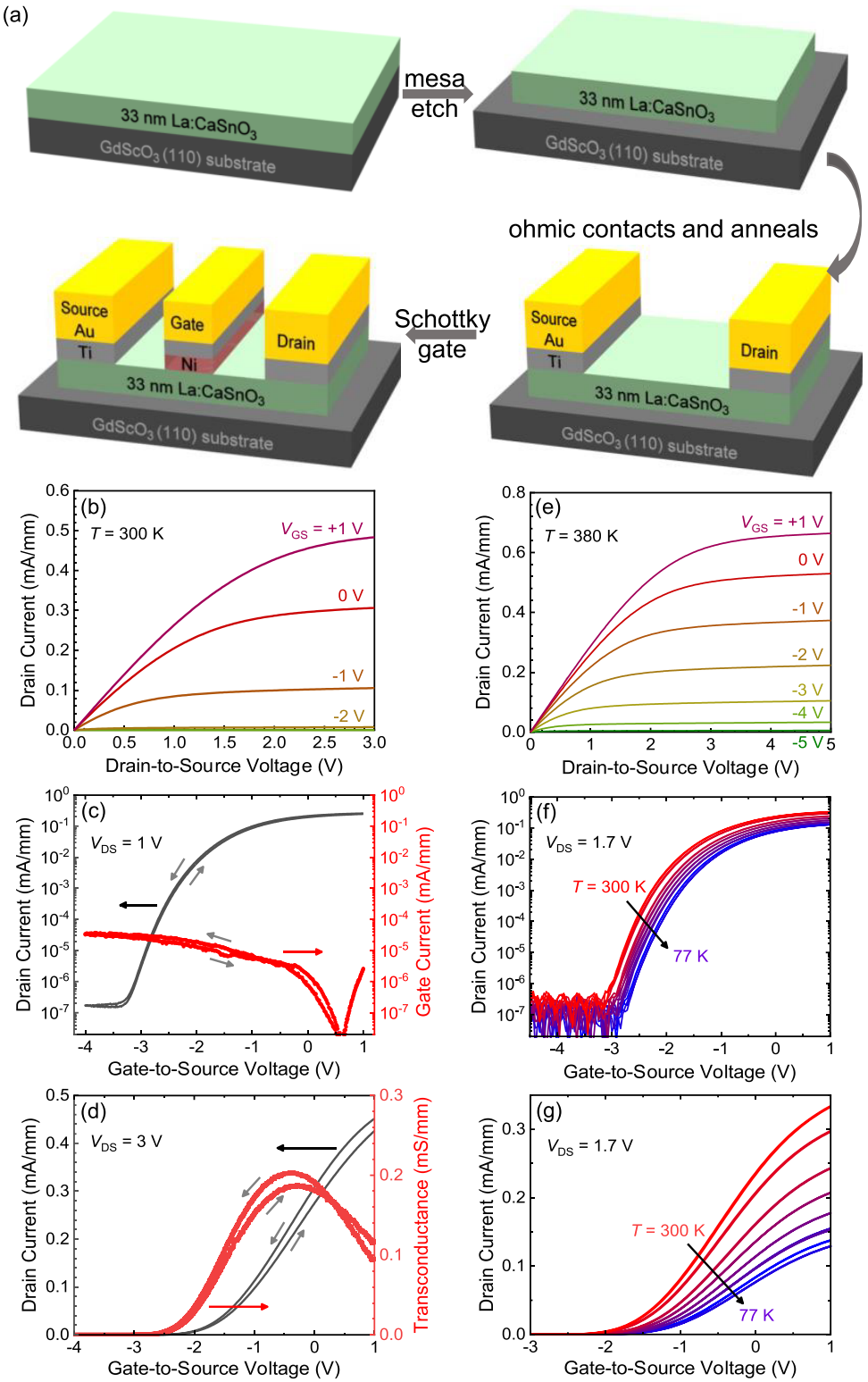

Figure 4. Fabrication and electrical characterization of the La:$CaSnO_3$ MESFET with L_{DS} = 9 μm , L_G = 3 μm, and W_{ch} = 50 μm. (a) Fabrication steps for the La:$CaSnO_3$ MESFETs. (b) Room-temperature drain current I_D versus drain-to-source voltage V_{DS} for the La:$CaSnO_3$ MESFET device for different gate-to-source voltages, V_{GS}. (c) Semilog plot of drain current I_D and gate current I_G versus gate-to-source V_{GS} for the same device at room temperature (d) Change in drain current and extrinsic transconductance with respect to gate-to-source voltage V_{GS} for the same device at room temperature. (e) Output characteristics at an elevated temperature of 380 K. (f, g) Temperature-dependent transfer characteristics at V_{DS} = 1.7 V on a (f) semilog plot and a (g) linear plot.

energy by expanding.[34] Table S1 compares this effect to previous observations in $SrTiO_3$,[34] showing that the effect is about 10 times larger than that of $SrTiO_3$.

Figure 3d shows the room-temperature Hall mobilities (μ_{300K}) as a function of carrier concentration n_{3D}. This result shows that the mobility increases with decreasing carrier

https://doi.org/10.1021/acsnano.3c04003
ACS Nano 2023, 17, 16912−16922

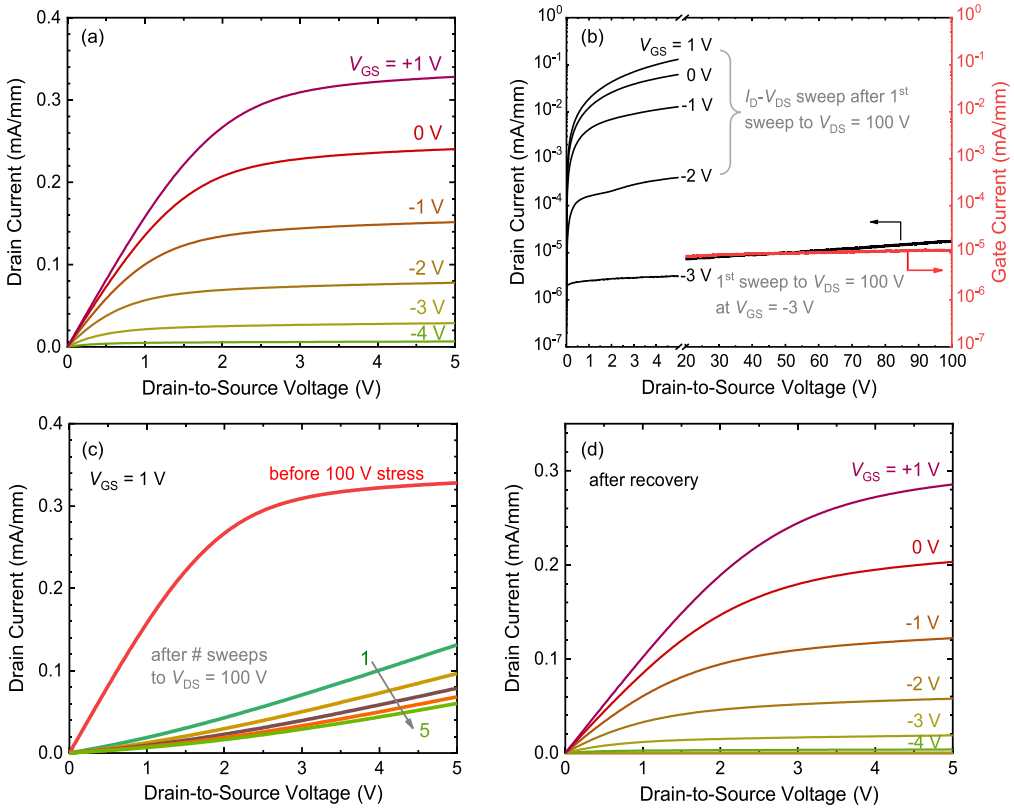

Figure 5. High-voltage performance of a $CaSnO_3$ MESFET with L_{DS} = 15 μm, L_G = 3 μm, and L_{GD} = 9 μm at 300K. (a) Output characteristics up to V_{DS} = 5 V for varying gate voltages V_{GS}. (b) Drain current I_D versus drain-to-source voltage V_{DS} for different gate-to-source voltages V_{GS} after sweeping the device to V_{DS} = 100 V in the off-state (V_{GS} = −3 V). The plot to the right shows the drain current and gate leakage current of the same device up to V_{DS} = 100 V in the off-state. (c) Output characteristics of a La:$CaSnO_3$ MESFET up to V_{DS} = 5 V taken before and after stressing the device to V_{DS} = 100 V in the off-state. The plot shows degradation of the drain current with each round of stress measurement. (d) Output characteristics of the device for varying gate voltages, V_{GS}, after a recovery time of ∼2 days, depicting current recovery to almost the same values as shown in (a).

concentration, a trend which is different from both $SrSnO_3$[27] and $BaSnO_3$.[5] Quantitatively, the maximum mobility of 42 $cm^2 V^{-1} s^{-1}$ is achieved at the *lowest* carrier concentration of 3.3 × 10^{19} cm^{-3}, and the *maximum conductivity* of 634 $S{\cdot}cm^{-1}$ is achieved at the *highest* carrier concentration of 1.6 × 10^{20} cm^{-3}.

One of the most attractive features of $CaSnO_3$ is its wide band gap. Previous studies have measured the band gap with diffuse reflectance to be ∼4.4 eV, and they have determined the band gap to be direct and the transition to be dipole-allowed.[2,3] Such a large direct band gap would be an exceptional asset to $CaSnO_3$, especially given the successful demonstration of doping in this study, as it may give rise to its application in UV optoelectronics. DFT calculations of the band structure of our strained films in Figure S8, predicts a *direct* gap of 4.19 eV (at Γ). This energy is only slightly less than the gap reported by Weston *et al.*[21] of 4.3 eV. To experimentally measure the band gap of our films, we performed spectroscopic ellipsometry. Figure S8 shows a reasonably good agreement between experiment and calculation, suggesting a direct band gap of ∼4.2 eV in strained $CaSnO_3$ films. However, to experimentally determine the band gap, we also fitted the absorption edge, as shown in Figure S9 for both undoped (Figure S9a) and doped (Figure S9b) films. These fittings yielded a direct gap of 4.64 eV, for the undoped sample, ∼0.2 eV greater than the gap previously measured for ceramic powders.[2,3] The direct gap of the doped film was found to be slightly larger, 4.68 eV. Future studies should be conducted to better understand this gap, perhaps using angle-resolved photoemission spectroscopy, and to manipulate the nature of this gap, possibly through strain engineering or chemical modification.

Ultimately, the goal of researching a semiconductor is to exploit its properties in an electronic device. To demonstrate the capability of $CaSnO_3$ for device operation, we fabricated metal−semiconductor field-effect transistors (MESFETs) by using $CaSnO_3$ as the channel material. The fabrication procedure is shown in Figure 4a, where the starting sample consisted of a 33-nm-thick La:$CaSnO_3$ film grown on a $GdScO_3$ (110) substrate with n_{3D} = 3.3 × 10^{19} cm^{-3}. Figure 4b shows the room-temperature output characteristics of a La:$CaSnO_3$ MESFET with source-to-drain spacing, L_{DS}, of 9 μm, gate length, L_G, of 3 μm, and width, W, of 50 μm. The drain current, I_D, at a gate-to-source voltage, V_{GS}, of +1 V is 0.48 mA/mm at a drain-to-source voltage, V_{DS}, of 3 V. The devices show linear turn-on characteristics and good saturation. The transfer characteristics of the same device are shown in Figure 4c. The MESFET operates in depletion mode and has a threshold voltage of −2.5 V. The on−off ratio is >10^6 and the off-state current is <10^{-6} mA/mm, where the off-state current is limited by leakage through the Schottky gate electrode. This behavior is expected in MESFET device geometry, where no gate insulator exists. The minimum subthreshold slope, SS, is 233 mV/dec, measured in the

https://doi.org/10.1021/acsnano.3c04003
ACS Nano 2023, 17, 16912−16922

current range between 10^{-6} and 10^{-5} mA/mm. The linear-mode transfer characteristics are shown in Figure 4d. Only a small hysteresis is observed between forward and reverse sweeps in this gate voltage range, and at V_{DS} = 3 V, the peak transconductance g_m was found to be ~0.2 mS/mm.

Temperature-dependent measurements were also performed on this device, and the results are shown in Figure 4e. Interestingly, the drive current improved to 0.62 mA/mm (0.68 mA/mm) at T = 380 K and V_{DS} = +3 (+5 V). Subthreshold measurements at different temperatures are shown in Figure 4f, where, surprisingly, the subthreshold slope did not decrease in proportion to temperature. While SS = 233 mV/dec at T = 300K, SS decreased to only 198 mV/dec at T = 77 K. Given the Schottky nature of the gate electrode, this could suggest that charge trapping in the bulk of La:$CaSnO_3$ plays a role in limiting the efficiency of the gate modulation. Another possibility could be the formation of an insulating layer at the Ni/La:$CaSnO_3$ surface. This possibility is supported by capacitance–voltage measurement (Figure S10), which shows that the capacitance saturates as the gate voltage is made more positive. This saturation is not expected in a MESFET and is more reminiscent of a metal-oxide field-effect transistor (MOSFET). This lower-than-expected gate capacitance is one possible reason for the low drive current in our devices. Finally, the temperature-dependent transfer characteristics are shown in Figure 4g, where I_D was found to decrease by roughly 1/2 going from 300K to 77 K. Since the film itself displays metallic behavior, as shown in the Hall measurements taken before fabrication in Figure S11, this temperature dependence must arise from the contacts. This, in turn, suggests that the contacts still have a thermionic component and that further improvement could be achieved by using a recessed gate design with higher doping in the contact regions, as previously demonstrated for $SrSnO_3$ MESFETs.[35]

Given the potential of $CaSnO_3$ for high-power devices due to its large band gap, we also performed high-voltage measurements on these devices. For these measurements, we chose a device with L_{DS} = 15 μm and L_G = 3 μm and gate-to-drain spacing, L_{GD}, of 9 μm. The room-temperature output characteristics of this device are shown in Figure 5a, where the measurements were taken before the application of high voltages. This device was initially measured out to V_{DS} = 5 V and displayed good saturation and slightly lower drive current than the device in Figure 4 owing to its longer L_{DS}. The high-voltage measurements are shown in Figure 5b. Here, the device was biased into the off-state (V_{GS} = −3 V), and then V_{DS} swept from 0 to 100 V, followed by a repeat of the I_D–V_{DS} measurements, which are also shown in the plot. The graph shows that the device did not suffer catastrophic breakdown and remained operational after the high-voltage pulse, though with decreased drive current. This procedure of applying V_{DS} = 100 V and then remeasuring the device at low voltage was repeated five times. The low-voltage on-state results (at V_{GS} = +1 V) after each set of repeated measurements are shown in Figure 5c. The drain current is seen to continue to decrease, though no catastrophic failure is observed, and the device structure remains intact. After performing these measurements, the device was stored in a vacuum for 2 days and then heated to T = 380 K and remeasured. These results are shown in Figure 5d, where it was observed that the device nearly completely recovered and showed a performance similar to the original measurements.

The current collapse observed at high voltages is similar to that observed in GaN high electron mobility transistors[36,37] and has been related to hot carriers filling traps either at the surface or in the bulk layers, which then deplete the channel, leading to reduced current. Therefore, in the future, techniques to minimize hot-carrier trapping, including the use of a field-plate geometry and surface passivation,[38] will be important to assess the ultimate high-voltage capabilities of $CaSnO_3$. Additionally, the role of ionic conduction in stannates[39] under high applied bias may also become an important factor and should be investigated.

DISCUSSION

A comparison of $CaSnO_3$'s doping behavior to those of the other alkaline earth stannates is illuminating. A plot of μ_{300K} versus n_{3D} is shown in Figure S12. The peak mobility in $CaSnO_3$ (42 cm^2 V^{-1} s^{-1}) is below that of $SrSnO_3$ (72.5 cm^2 V^{-1} s^{-1})[7] and $BaSnO_3$ (120 cm^2 V^{-1} s^{-1})[5] grown with the same technique. This is explained by the smaller band dispersion of $CaSnO_3$ resulting in a heavier conduction band effective mass (m^*).[2] We note that, in these highly polar materials, an increase in m^* can cause polaronic effects that amplify its effect on mobility beyond the proportionality implied by the Drude formula.[40] Finally, we point out the qualitative differences in μ_{300K} versus n_{3D} apparent in Figure S12. Thin-film $BaSnO_3$ has a mostly positive correlation between dopant concentration and mobility due to the carriers screening charged dislocation scattering,[5,6] and $SrSnO_3$'s mobility is nearly independent of carrier concentration due to phonon scattering dominating the room-temperature mobility.[27] However, $CaSnO_3$ has a mobility that is *negatively* correlated with the carrier concentration. This behavior is typically seen in extremely pure high-quality crystals such as Si[41] and suggests a low defect concentration where electrons are predominantly scattered by the ionized La donors themselves.

The fact that we achieved successful n-type doping of $CaSnO_3$ without facing any major obstacles raises the question, Why did previous attempts fail? The most noteworthy attempt was by Wei *et al.*, who deposited $La_{0.03}Ca_{0.97}SnO_3$ with PLD and failed to achieve measurable conductivity.[20] There are four major differences between this study and our own: (1) Wei *et al.* used highly lattice-mismatched (−3.2%) and tilt-mismatched (>6°) $LaAlO_3$ substrates, whereas this study used closely lattice-matched $GdScO_3$ substrates. (2) Wei *et al.* used PLD, whereas this study used hybrid MBE. (3) Wei *et al.* used a substrate temperature of 750 °C, whereas we used a much higher substrate temperature of 950 °C. (4) Wei *et al.* used a doping fraction fixed at 3% in their target, whereas we used an effusion cell at various temperatures to introduce La. Both high lattice mismatch and high-energy ions from PLD are known to introduce defects that could conceivably compensate carriers and lead to insulating films in their study.

It is also interesting to discuss how the doping limitations of $CaSnO_3$ affect the device performance and what avenues for improvement are possible. While the La:$CaSnO_3$ MESFETs in this study demonstrate the basic capabilities of field-effect transistors based on $CaSnO_3$, a considerable increase in the performance is needed. The low drive current is a result of (1) the relatively low channel doping, which limits the intrinsic current carrying capacity of the devices, and (2) the high contact resistance (~500 Ω-mm), which is also a result of the low doping. Much higher doping is needed to create tunneling

https://doi.org/10.1021/acsnano.3c04003
ACS Nano 2023, 17, 16912–16922

contacts, and the use of a thinner channel region and a recessed-gate geometry[35] could allow devices to achieve higher drive current and transconductance. An estimate of the field-effect mobility in our devices was obtained from the intrinsic g_m (0.22 mS/mm) and the device capacitance which yielded an apparent field-effect mobility, μ_{FE}, of 1.2 $cm^2/(V\ s)$. However, this value does not reflect the true transport mobility of $CaSnO_3$, due to the high contact resistance and nonideal device geometry ($L_G \ll L_{DS}$) for mobility extraction. Future experiments using more suitable device geometries are needed in order to determine an accurate value of μ_{FE}. While this work shows that controllable doping is possible, the performance did vary between different devices on this wafer. Figure S13 shows the I_D-V_{GS} characteristics of several devices fabricated on the same wafer, and Table S2 lists the device parameters and performance metrics. We attribute these differences primarily to variations in the contacts and not the intrinsic material properties, since at these doping levels even small variations in the dopant concentration and interfacial properties can lead to large variations in contact resistance.

OUTLOOK

We suggest four directions for future work. First, studies should be carried out to precisely understand what mechanisms limit the doping concentrations and mobilities of these doped films. This might include identifying compensation mechanisms that prevent dilute doping, understanding whether self-compensation or secondary phase precipitation processes prevent heavier doping, and precisely resolving electron scattering mechanisms. If these limiting factors can be understood and rectified, then higher mobilities and a wider range of doping concentrations can be achieved. Second, given the direct band gap of strained $CaSnO_3$ films, $CaSnO_3$ may find applications in UV optoelectronics. Since most advanced optoelectronic devices are bipolar, the exploration of p-type doping strategies, as already done for $BaSnO_3$,[42,43] might be a next step. Third, successful doping in $CaSnO_3$ raises the question of whether other materials previously thought to be undopable can be doped. Specifically, $MgSnO_3$ and $ZnSnO_3$ are metastable perovskites that have been epitaxially stabilized,[44] but never doped. Finally, $CaSnO_3$ should be explored as a component in heterostructures, for instance, by serving as a wide-band-gap modulation donor to perovskites with similar lattice parameters.

CONCLUSIONS

This study demonstrates the adsorption-controlled growth of $CaSnO_3$—a material previously deemed undopable—with controllable doping using hybrid MBE. Chemical doping resulted in 100% dopant activation with free electron concentrations ranging from 3.3×10^{19} to 1.6×10^{20} cm^{-3}. A maximum room-temperature mobility of 42 $cm^2\ V^{-1}\ s^{-1}$ at $n_{3D} = 3.3 \times 10^{19}$ cm^{-3} was achieved. Despite comparable ionic radii of La, increasing the doping concentration resulted in an expansion of the out-of-plane lattice parameters, which is attributed to an electronic effect based on the DFT calculations. The surprising robustness and predictability of the doping also allowed us to fabricate and demonstrate the operation of $CaSnO_3$-based field-effect transistors. These results encourage revisiting $CaSnO_3$ as a viable ultrawide-band-gap semiconductor for devices.

EXPERIMENTAL SECTION

Film Growth. The La:$CaSnO_3$ thin films were grown by using hybrid molecular beam epitaxy (hMBE). This approach employs conventional effusion cells for lanthanum and calcium, hexamethylditin (HMDT) as a metal−organic precursor for tin, and an inductively coupled RF plasma for oxygen. The reader is referred to Prakash *et al.* for more details about the technique as applied to $BaSnO_3$.[24] Figure S14 summarizes the technique as applied to La:$CaSnO_3$. All films were grown on $GdScO_3$ (110) single-crystal substrates, indexed in the *Pbnm* setting (CrysTec GmbH). All films were grown at a fixed substrate temperature of 950 °C as measured with a floating thermocouple. The substrates were cleaned *in situ* with oxygen plasma for 25 min prior to film deposition. Ca was sublimed from a titanium crucible with its BEP fixed at 2.65×10^{-8} mbar, as measured by a retractable beam flux monitor before growth. The oxygen flow was set to 0.7 standard cubic centimeters per minute (sccm) to achieve an oxygen background pressure of 5×10^{-6} Torr while applying 250 W of RF power to the plasma coil. These conditions achieved a growth rate of 22 nm per hour.

HMDT vapor entered the chamber through a heated gas injector (E-Science, Inc.) in an effusion cell port that was in direct line-of-sight with the substrate. The HMDT vapor reached the injector *via* a linear leak valve followed by a capacitance manometer (Baratron, MKS Instruments, Inc.), the valve opening serving as the control variable and the manometer pressure serving as the process variable in a control loop. The HMDT bubbler was held at ∼75 °C to provide sufficient HMDT vapor pressure, and the HMDT vapor lines were held at a slightly higher temperature of ∼85 °C to prevent HMDT condensation in the lines. Temperatures were controlled with resistive heating tape powered by autotransformers, and the temperatures were monitored with grounded thermocouples tack-welded to the crucible or lines. The injector itself was held at 60 °C.

Cation stoichiometry (Sn:Ca ratio) was explored by varying the HMDT manometer set point pressure from 200 to 240 mTorr, which achieved a BEP of 2.33×10^{-5} to 3.07×10^{-5} mbar. A gas sensitivity factor of 1.0 (relative to nitrogen calibration) was used, equal to that used for Ca. Each film during stoichiometry optimization was grown for 180 min. La was used as a dopant motivated by the similar ionic radii of La^{3+} and Ca^{2+} (Figure S7). To introduce La, a tantalum-crucible high-temperature effusion cell was used (Dr. Eberl-MBE Komponenten GmbH). During cation stoichiometry optimization, the La cell temperature was fixed at 1190 °C to provide carriers whose mobilities could be used to infer stoichiometry. The carrier density was then varied by changing the La cell temperature from 1120 to 1205 °C. Each film was grown for 90 min.

Film Characterization. A Rigaku SmartLab XE instrument was used for X-ray scattering measurements. Film thicknesses were extracted from the X-ray reflectivity (XRR). Reciprocal space maps (RSMs) were collected by scanning ω while using the HyPix-3000 detector in one-dimensional mode to simultaneously resolve 2θ. Electric transport measurements were performed in a Quantum Design physical property measurement system (DynaCool) using aluminum wire that bonds directly to the film in the van der Pauw geometry.

STEM specimens were prepared using a Thermo Fisher Scientific Helios G4 UX focused ion beam (FIB) with standard lift-out and thinning methods for imaging the $[001]_{orth}$ zone axis. STEM imaging and EELS mapping were performed on a Thermo Fisher Scientific Spectra 300 X-CFEG operating at 300 kV with a convergence angle of 30 mrad. The inner and outer collection angles for HAADF-STEM imaging were approximately 60 and 200 mrad, respectively. All images were acquired as series of fast acquisitions and subsequently aligned and summed to produce high signal-to-noise ratio images while minimizing scan artifacts. EEL spectra were acquired with a Gatan Continuum system equipped with a scintillator CMOS camera. Each spectrum was background-subtracted, and the relevant elemental edges were summed to produce elemental maps.

Ellipsometry measurements were done on a J. A. Woollam M-2000 at Drexel University. The light source was composed of a deuterium

https://doi.org/10.1021/acsnano.3c04003
ACS Nano 2023, 17, 16912−16922

lamp and a QTH lamp, allowing measurements over wavelengths from 210 to 1650 nm. A bare $GdScO_3$ substrate as well as the samples were measured at five different incident angles (65, 67.5, 70, 72.5, and 75 degrees). The results were modeled using CompleteEASE software, first for the substrate and then for the film + substrate data, obtaining refractive index n and extinction coefficient k values, using film thickness as an input.

Device Fabrication. The MESFET fabrication procedure started by using optical lithography to define the active device area, and Ar^+ ion milling was performed for 15 min to create the mesa regions. The mesa was intentionally overetched to ensure the La:$CaSnO_3$ was completely removed in the field regions. After mesa isolation, a second optical lithography cycle was performed and source/drain (S/D) contacts were defined, followed by evaporation of 100 nm Au/75 nm Ti using electron-beam evaporation. After solvent lift-off, two-terminal $I-V$ curves were taken for the S/D contacts to determine the quality of the contacts. The contacts were initially observed to have high resistance and were therefore annealed at a series of increasing temperatures until good ohmic behavior was observed, similar to previous studies on $SrSnO_3$.[45] These anneals were performed in an N_2 environment at sequential temperatures of 200, 300, and 320 °C for 6.5 min each. After each anneal, two-terminal $I-V$ curves of the S/D contacts were taken to monitor the improvement in current injection into the contacts. The on-resistance improved from ∼951 kΩ-mm in the as-deposited contacts to 1.22 kΩ-mm at 300 °C, while no further improvement was seen after the 320 °C anneal. The results of these measurements are described in the Supporting Information Figure S15. After the S/D contact annealing experiments were completed, optical lithography was used again to pattern the Schottky gate electrodes, followed by 80 nm Au/10 nm Ti/90 nm Ni evaporation and solvent lift-off. After fabrication, the devices were measured using a Keysight B1500 semiconductor parameter analyzer under a vacuum at $\sim 2 \times 10^{-6}$ Torr.

Density Functional Theory Calculations. The calculations are based on density functional theory[46,47] and the HSE06 hybrid functional[48,49] as implemented in the VASP code.[50] The interactions between valence electrons and ionic cores were treated using the projector-augmented potential (PAW) method,[51] with the following valence configurations: Ca: $3p^6 4s^2$, Sn: $5s^2 5p^2$, O: $2s^2 2p^2$, La: $5s^2 5p^6 6s^2\ 5d^1$. We used the standard mixing parameter of 25% in the HSE06 and a plane wave cutoff of 500 eV. Within the generalized gradient approximation revised for solids, PBEsol, we performed calculations adding one electron to supercells of 40 and 320 atoms, representing concentrations of 2.0×10^{21} cm^{-3} and 2.5×10^{20} cm^{-3}, using only the Γ point for integrations over the Brillouin zone. The simulations of the epitaxially strained doped and undoped $CaSnO_3$ were carried out by having the $[1\bar{1}0]_{orth}$ and $[001]_{orth}$ and as a and b in-plane lattice vectors constrained to the substrate lattice parameters and allowing the out-of-plane c lattice parameter along the $[110]_{orth}$ direction to relax. The in-plane lattice parameters a and b were expanded by +0.48% and +0.67% with respect to their theoretical equilibrium lattice parameter to represent the tensile stress from the deposition on the $GdScO_3$ substrate, also with $[110]_{orth}$ as the out-of-plane direction.

To investigate the pure electronic effect, we performed calculations by adding only one extra electron to the supercell of perfect bulk $CaSnO_3$ and allowing the c-axis ($[110]_{orth}$) to relax; for the pure size effect, we replaced one Ca with one La, removed the extra electron that would populate the conduction band minimum, and allowed the c-axis to relax; and for the combined electronic and size effects, we performed calculations by replacing one Ca with La, including the extra electron in the conduction band, and allowing the c-axis to relax.

ASSOCIATED CONTENT

Supporting Information

The Supporting Information is available free of charge at https://pubs.acs.org/doi/10.1021/acsnano.3c04003.

Structural characterization, optical measurements, temperature-dependent transport measurements, additional device results, and band structure calculations (PDF)

AUTHOR INFORMATION

Corresponding Authors

Steven J. Koester − *Department of Electrical and Computer Engineering, University of Minnesota−Twin Cities, Minneapolis, Minnesota 55455, United States;* orcid.org/0000-0001-6104-1218; Email: skoester@umn.edu

Bharat Jalan − *Department of Chemical Engineering and Materials Science, University of Minnesota−Twin Cities, Minneapolis, Minnesota 55455, United States;* orcid.org/0000-0002-7940-0490; Email: bjalan@umn.edu

Authors

Fengdeng Liu − *Department of Chemical Engineering and Materials Science, University of Minnesota−Twin Cities, Minneapolis, Minnesota 55455, United States*

Prafful Golani − *Department of Electrical and Computer Engineering, University of Minnesota−Twin Cities, Minneapolis, Minnesota 55455, United States;* orcid.org/0000-0002-9215-0107

Tristan K. Truttmann − *Department of Chemical Engineering and Materials Science, University of Minnesota−Twin Cities, Minneapolis, Minnesota 55455, United States*

Igor Evangelista − *Department of Materials Science and Engineering, University of Delaware, Newark, Delaware 19716, United States;* orcid.org/0000-0003-2402-9484

Michelle A. Smeaton − *Department of Materials Science and Engineering, Cornell University, Ithaca, New York 14853, United States;* orcid.org/0000-0001-9114-1009

David Bugallo − *Department of Materials Science and Engineering, Drexel University, Philadelphia, Pennsylvania 19104, United States; Centro de Investigación en Química Biolóxica e Materiais Moleculares (CIQUS), Universidade de Santiago de Compostela, Santiago de Compostela 15782, Spain*

Jiaxuan Wen − *Department of Electrical and Computer Engineering, University of Minnesota−Twin Cities, Minneapolis, Minnesota 55455, United States*

Anusha Kamath Manjeshwar − *Department of Chemical Engineering and Materials Science, University of Minnesota−Twin Cities, Minneapolis, Minnesota 55455, United States*

Steven J. May − *Department of Materials Science and Engineering, Drexel University, Philadelphia, Pennsylvania 19104, United States*

Lena F. Kourkoutis − *School of Applied and Engineering Physics and Kavli Institute at Cornell for Nanoscale Science, Cornell University, Ithaca, New York 14853, United States;* orcid.org/0000-0002-1303-1362

Anderson Janotti − *Department of Materials Science and Engineering, University of Delaware, Newark, Delaware 19716, United States;* orcid.org/0000-0002-0358-2101

Complete contact information is available at: https://pubs.acs.org/10.1021/acsnano.3c04003

Author Contributions

F.L. and P.G. are both equally contributing authors. F.L., P.G., T.K.T., S.J.K., and B.J. conceived the idea and designed experiments. Films were grown and characterized with XRD

https://doi.org/10.1021/acsnano.3c04003
ACS Nano 2023, 17, 16912−16922

and AFM by F.L. and T.K.T. Electrical transport measurements were performed by F.L. and A.K.M. Transistor fabrication was performed by P.G., while electrical testing was done by P.G. and J.W. under the supervision of S.J.K. STEM measurements were done by M.A.S. under the guidance of L.F.K. I.E. performed DFT calculations under the direction of A.J. Ellipsometry measurements were done by D.B., and diffraction simulations were carried out by S.J.M. F.L., P.G., and T.K.T. wrote the manuscript with input from all authors. B.J. and S.J.K. directed and organized the materials and device aspects of the project, respectively.

Notes

The authors declare no competing financial interest.

ACKNOWLEDGMENTS

The work was primarily supported by the Air Force Office of Scientific Research (AFOSR) through grants FA9550-19-1-0245, FA9550-21-1-0025, and FA9550-21-0460. We acknowledge partial support from the National Science Foundation (NSF) through award number DMR-2306273. We (S.J.K., B.J., and S.J.M.) also acknowledge partial support from the NSF through the Future of Semiconductor teaming grant (FuSe-TG) (award no. DMR-2235208). Film growth was performed using instrumentation funded by AFOSR DURIP award FA9550-18-1-0294. Parts of this work were carried out in the Characterization Facility, University of Minnesota, which receives partial support from the NSF through the MRSEC (award no. DMR-2011401). Portions of this work were carried out at the Minnesota Nano Center, which receives support from the NSF through the National Nanotechnology Coordinated Infrastructure (NNCI) under award no. ECCS-2025124. D.B. acknowledges the funding received from the European Union through the Marie Skłodowska-Curie Actions Postdoctoral Fellowship (ref 101063432). Transmission electron microscopy work was supported by the NSF [Platform for the Accelerated Realization, Analysis, and Discovery of Interface Materials (PARADIM)] under Cooperative Agreement No. DMR-2039380 and made use of the Cornell Center for Materials Research (CCMR) Shared Facilities, which are supported through the NSF MRSEC Program (DMR-1719875). M.A.S. acknowledges support from the NSF GRFP (DGE-2139899). I.E. was supported by the EERE Solar Energy Technologies Office, DOE grant number DE-EE0009344. A.J. was supported by the NSF through the UD-CHARM University of Delaware MRSEC Center (no. DMR-2011824) and acknowledge the use of Bridges-2 at PSC through allocation DMR150099 from the Advanced Cyberinfrastructure Coordination Ecosystem: Services & Support (ACCESS) program and the DARWIN computing system at the University of Delaware, which is supported by the NSF grant number 1919839.

REFERENCES

(1) Kim, H. J.; Kim, U.; Kim, H. M.; Kim, T. H.; Mun, H. S.; Jeon, B.-G.; Hong, K. T.; Lee, W.-J.; Ju, C.; Kim, K. H.; Char, K. High Mobility in a Stable Transparent Perovskite Oxide. *Applied Physics Express* **2012**, *5* (6), No. 061102.

(2) Mizoguchi, H.; Eng, H. W.; Woodward, P. M. Probing the Electronic Structures of Ternary Perovskite and Pyrochlore Oxides Containing Sn^{4+} Or Sb^{5+}. *Inorg. Chem.* **2004**, *43* (5), 1667−1680.

(3) Zhang, W.; Tang, J.; Ye, J. Structural, Photocatalytic, and Photophysical Properties of Perovskite $MSnO_3$ (M = Ca, Sr, And Ba) Photocatalysts. *J. Mater. Res.* **2007**, *22* (7), 1859−1871.

(4) Paik, H.; Chen, Z.; Lochocki, E.; Seidner, H. A.; Verma, A.; Tanen, N.; Park, J.; Uchida, M.; Shang, S.; Zhou, B.-C.; Brützam, M.; Uecker, R.; Liu, Z.-K.; Jena, D.; Shen, K. M.; Muller, D. A.; Schlom, D. G. Adsorption-Controlled Growth of La-Doped $BaSnO_3$ by Molecular-Beam Epitaxy. *APL Materials* **2017**, *5* (11), No. 116107.

(5) Prakash, A.; Xu, P.; Faghaninia, A.; Shukla, S.; Ager, J. W.; Lo, C. S.; Jalan, B. Wide Bandgap $BaSnO_3$ Films with Room Temperature Conductivity Exceeding 10^4 S cm^{-1}. *Nat. Commun.* **2017**, *8* (1), 15167.

(6) Mun, H.; Kim, U.; Min Kim, H.; Park, C.; Hoon Kim, T.; Joon Kim, H.; Hoon Kim, K.; Char, K. Large Effects of Dislocations on High Mobility of Epitaxial Perovskite $Ba_{0.96}La_{0.04}SnO_3$ Films. *Appl. Phys. Lett.* **2013**, *102* (25), No. 252105.

(7) Truttmann, T. K.; Liu, F.; Garcia-Barriocanal, J.; James, R. D.; Jalan, B. Strain Relaxation via Phase Transformation in High-Mobility $SrSnO_3$ Films. *ACS Applied Electronic Materials* **2021**, *3* (3), 1127−1132.

(8) Chaganti, V. R. S. K.; Prakash, A.; Yue, J.; Jalan, B.; Koester, S. J. Demonstration of a Depletion-Mode $SrSnO_3$ n-Channel MESFET. *IEEE Elec. Dev. Lett.* **2018**, *39* (9), 1381.

(9) Wen, J.; Chaganti, V. R. S. K.; Truttmann, T. K.; Liu, F.; Jalan, B.; Koester, S. J. $SrSnO_3$ Metal-Semiconductor Field-Effect Transistor with GHz Operation. *IEEE Elect. Dev. Lett.* **2021**, *42* (1), 74−77.

(10) Wang, T.; Thoutam, L. R.; Prakash, A.; Nunn, W.; Haugstad, G.; Jalan, B. Defect-Driven Localization Crossovers in MBE-Grown La-Doped $SrSnO_3$ Films. *Physical Review Materials* **2017**, *1* (6), No. 061601.

(11) Wang, T.; Prakash, A.; Dong, Y.; Truttmann, T.; Bucsek, A.; James, R.; Fong, D. D.; Kim, J.-W.; Ryan, P. J.; Zhou, H.; Birol, T.; Jalan, B. Engineering $SrSnO_3$ Phases and Electron Mobility at Room Temperature Using Epitaxial Strain. *ACS Appl. Mater. Interfaces* **2018**, *10* (50), 43802−43808.

(12) Truttmann, T.; Prakash, A.; Yue, J.; Mates, T. E.; Jalan, B. Dopant Solubility and Charge Compensation in La-Doped $SrSnO_3$ Films. *Appl. Phys. Lett.* **2019**, *115* (15), No. 152103.

(13) Glerup, M.; Knight, K. S.; Poulsen, F. W. High Temperature Structural Phase Transitions in $SrSnO_3$ Perovskite. *Mater. Res. Bull.* **2005**, *40* (3), 507−520.

(14) Mountstevens, E. H.; Attfield, J. P.; Redfern, S. A. T. Cation-Size Control of Structural Phase Transitions in Tin Perovskites. *J. Phys.: Condens. Matter* **2003**, *15* (49), 8315−8326.

(15) Redfern, S. A. T.; Chen, C. J.; Kung, J.; Chaix-Pluchery, O.; Kreisel, J.; Salje, E. K. H. Raman Spectroscopy of $CaSnO_3$ at High Temperature: a Highly Quasi-Harmonic Perovskite. *J. Phys.: Condens. Matter* **2011**, *23* (42), No. 425401.

(16) Schneider, B. W.; Liu, W.; Li, B. Searching for Post-Perovskite Transition in $CaSnO_3$ at High Pressure: an Ultrasonic Velocity Study to 18 GPa. *High Pressure Research* **2008**, *28* (3), 397−404.

(17) Tateno, S.; Hirose, K.; Sata, N.; Ohishi, Y. Structural Distortion of $CaSnO_3$ Perovskite Under Pressure and the Quenchable Post-Perovskite Phase as a Low-Pressure Analogue to $MgSiO_3$. *Physics of the Earth and Planetary Interiors* **2010**, *181* (1), 54−59.

(18) Liferovich, R. P.; Mitchell, R. H. A Structural Study of Ternary Lanthanide Orthoscandate Perovskites. *J. Solid State Chem.* **2004**, *177* (6), 2188−2197.

(19) Baliga, B. J. Semiconductors For High-Voltage, Vertical Channel Field-Effect Transistors. *J. Appl. Phys.* **1982**, *53* (3), 1759−1764.

(20) Wei, M.; Cho, H. J.; Ohta, H. Tuning of the Optoelectronic Properties for Transparent Oxide Semiconductor $ASnO_3$ by Modulating the Size of A-Ions. *ACS Applied Electronic Materials* **2020**, *2* (12), 3971−3976.

(21) Weston, L.; Bjaalie, L.; Krishnaswamy, K.; Van de Walle, C. G. Origins of *n*-Type Doping Difficulties in Perovskite Stannates. *Phys. Rev. B* **2018**, *97* (5), No. 054112.

(22) Shaili, H.; Salmani, E.; Beraich, M.; Zidane, M.; Taibi, M. h.; Rouchdi, M.; Ez-Zahraouy, H.; Hassanain, N.; Mzerd, A. Higher Conductivity and Enhanced Optoelectronic Properties of Chemically

https://doi.org/10.1021/acsnano.3c04003
ACS Nano 2023, 17, 16912−16922

Grown Nd-Doped $CaSnO_3$ Perovskite Oxide Thin Films. *ACS Omega* **2021**, *6* (48), 32537−32547.
(23) Liu, Q.; Jin, F.; Li, B.; Geng, L. Structure and Band Gap Energy of $CaSnO_3$ Epitaxial Films on $LaAlO_3$ Substrate. *J. Alloys Compd.* **2017**, *717*, 55−61.
(24) Prakash, A.; Xu, P.; Wu, X.; Haugstad, G.; Wang, X.; Jalan, B. Adsorption-Controlled Growth and the Influence of Stoichiometry on Electronic Transport in Hybrid Molecular Beam Epitaxy-Grown $BaSnO_3$ Films. *Journal of Materials Chemistry C* **2017**, *5* (23), 5730−5736.
(25) Dirsyte, R.; Schwarzkopf, J.; Wagner, G.; Fornari, R.; Lienemann, J.; Busch, M.; Winter, H. Thermal-Induced Change in Surface Termination Of $DyScO_3$(110). *Surf. Sci.* **2010**, *604* (21), L55−L58.
(26) Kleibeuker, J. E.; Koster, G.; Siemons, W.; Dubbink, D.; Kuiper, B.; Blok, J. L.; Yang, C.-H.; Ravichandran, J.; Ramesh, R.; ten Elshof, J. E.; Blank, D. H. A.; Rijnders, G. Atomically Defined Rare-Earth Scandate Crystal Surfaces. *Adv. Funct. Mater.* **2010**, *20* (20), 3490−3496.
(27) Truttmann, T. K.; Zhou, J.-J.; Lu, I. T.; Rajapitamahuni, A. K.; Liu, F.; Mates, T. E.; Bernardi, M.; Jalan, B. Combined Experimental-Theoretical Study of Electron Mobility-Limiting Mechanisms in $SrSnO_3$. *Communications Physics* **2021**, *4* (1), 241.
(28) Mott, N. F. The Minimum Metallic Conductivity. *Int. Rev. Phys. Chem.* **1985**, *4* (1), 1−18.
(29) Allen, S. J.; Raghavan, S.; Schumann, T.; Law, K.-M.; Stemmer, S. Conduction Band Edge Effective Mass of La-Doped $BaSnO_3$. *Appl. Phys. Lett.* **2016**, *108* (25), No. 252107.
(30) Nunn, W.; Prakash, A.; Bhowmik, A.; Haislmaier, R.; Yue, J.; Garcia Lastra, J. M.; Jalan, B. Frequency- and Temperature-Dependent Dielectric Response in Hybrid Molecular Beam Epitaxy-Grown $BaSnO_3$ Films. *APL Mater.* **2018**, *6* (6), No. 066107.
(31) Trari, M.; Doumerc, J.-P.; Dordor, P.; Pouchard, M.; Behr, G.; Krabbes, G. Preparation and Characterization of Lanthanum Doped $BaSnO_3$. *J. Phys. Chem. Solids* **1994**, *55* (11), 1239−1243.
(32) Glavic, A.; Bjorck, M. GenX 3: The Latest Generation of an Established Tool. *J. Appl. Crystallogr.* **2022**, *55* (4), 1063−1071.
(33) Van de Walle, C. G.; Martin, R. M. "Absolute" Deformation Potentials: Formulation and Ab Initio Calculations For Semiconductors. *Phys. Rev. Lett.* **1989**, *62* (17), 2028−2031.
(34) Janotti, A.; Jalan, B.; Stemmer, S.; Van de Walle, C. G. Effects of Doping on the Lattice Parameter of $SrTiO_3$. *Appl. Phys. Lett.* **2012**, *100* (26), No. 262104.
(35) Chaganti, V. R. S. K.; Truttmann, T. K.; Liu, F.; Jalan, B.; Koester, S. J. $SrSnO_3$ Field-Effect Transistors with Recessed Gate Electrodes. *IEEE Electron Device Lett.* **2020**, *41* (9), 1428−1431.
(36) Vetury, R.; Zhang, N. Q.; Keller, S.; Mishra, U. K. The Impact of Surface States on the DC And RF Characteristics of AlGaN/GaN HFETs. *IEEE Trans. Electron Devices* **2001**, *48* (3), 560−566.
(37) Mizutani, T.; Ohno, Y.; Akita, M.; Kishimoto, S.; Maezawa, K. A Study on Current Collapse In AlGaN/GaN HEMTs Induced by Bias Stress. *IEEE Trans. Electron Devices* **2003**, *50* (10), 2015−2020.
(38) Jiang, H.; Liu, C.; Chen, Y.; Lu, X.; Tang, C. W.; Lau, K. M. Investigation of In Situ SiN as Gate Dielectric And Surface Passivation for GaN MISHEMTs. *IEEE Trans. Electron Devices* **2017**, *64* (3), 832−839.
(39) Belthle, K. S.; Gries, U. N.; Mueller, M. P.; Kemp, D.; Prakash, A.; Rose, M. A.; Börgers, J. M.; Jalan, B.; Gunkel, F.; Souza, R. A. D. Quantitative Determination of Native Point-Defect Concentrations at the ppm Level in Un-Doped $BaSnO_3$ Thin Films. *Adv. Funct. Mater.* **2022**, *32* (19), No. 2113023.
(40) Zhou, J.-J.; Bernardi, M. Predicting Charge Transport in the Presence of Polarons: the Beyond-Quasiparticle Regime in $SrTiO_3$. *Physical Review Research* **2019**, *1* (3), No. 033138.
(41) Mousty, F.; Ostoja, P.; Passari, L. Relationship between Resistivity and Phosphorus Concentration in Silicon. *J. Appl. Phys.* **1974**, *45* (10), 4576−4580.
(42) Kim, H. M.; Kim, U.; Park, C.; Kwon, H.; Char, K. Thermally Stable pn-Junctions Based on a Single Transparent Perovskite Semiconductor $BaSnO_3$. *APL Materials* **2016**, *4* (5), No. 056105.
(43) Wang, J.; Luo, B. Electronic Properties of p-Type $BaSnO_3$ Thin Films. *Ceram. Int.* **2020**, *46* (16), 25678−25682.
(44) Fujiwara, K.; Minato, H.; Shiogai, J.; Kumamoto, A.; Shibata, N.; Tsukazaki, A. Thin-Film Stabilization Of $LiNbO_3$-Type $ZnSnO_3$ And $MgSnO_3$ by Molecular-Beam Epitaxy. *APL Materials* **2019**, *7* (2), No. 022505.
(45) Chaganti, V. R. S. K.; Golani, P.; Truttmann, T. K.; Liu, F.; Jalan, B.; Koester, S. J. Optimizing Ohmic Contacts to Nd-Doped n-Type $SrSnO_3$. *Appl. Phys. Lett.* **2021**, *118* (14), No. 142104.
(46) Kohn, W.; Sham, L. J. Self-Consistent Equations Including Exchange and Correlation Effects. *Phys. Rev.* **1965**, *140* (4A), A1133−A1138.
(47) Hohenberg, P.; Kohn, W. Inhomogeneous Electron Gas. *Phys. Rev.* **1964**, *136* (3B), B864−B871.
(48) Heyd, J.; Scuseria, G. E.; Ernzerhof, M. Hybrid Functionals Based on a Screened Coulomb Potential. *J. Chem. Phys.* **2003**, *118* (18), 8207−8215.
(49) Paier, J.; Marsman, M.; Hummer, K.; Kresse, G.; Gerber, I. C.; Ángyán, J. G. Erratum: "Screened Hybrid Density Functionals Applied to Solids. *J. Chem. Phys.* **2006**, *125* (24), No. 249901.
(50) Kresse, G.; Furthmüller, J. Efficient Iterative Schemes for Ab Initio Total-Energy Calculations Using a Plane-Wave Basis Set. *Phys. Rev. B* **1996**, *54* (16), 11169−11186.
(51) Kresse, G.; Joubert, D. From Ultrasoft Pseudopotentials to the Projector Augmented-Wave Method. *Phys. Rev. B* **1999**, *59* (3), 1758−1775.

https://doi.org/10.1021/acsnano.3c04003
ACS Nano 2023, 17, 16912−16922